

Spectral analysis of the Koopman operator recovers Hamiltonian parameters in open quantum systems

Jorge E. Pérez-García, Carlos Colchero, and Julio C. Gutiérrez-Vega*

*Photonics and Mathematical Optics Group,
Tecnológico de Monterrey, Monterrey, 64849, México.*

(Dated: December 1, 2025)

An accurate identification of Hamiltonian parameters is essential for modeling and control of open quantum systems. In this work, a novel data-driven method for inferring such parameters from first-moment dynamics is presented using an open 2D quantum harmonic oscillator as an example. The method relies on the discrete spectrum of the Koopman operator to obtain such parameters, which is obtained using the multichannel Hankel Alternative View of Koopman (mHAVOK) algorithm; a theoretical connection of such affirmation is presented. The method is tested on the expected value of noiseless quadratures, retrieving oscillation frequencies, damping rates, nonlinear Kerr shifts, qubit-photon coupling strengths of a Jaynes-Cummings interaction, and a modulated frequency of a time-dependent Hamiltonian. The majority of the recovered parameters remained within 5% of their true values. When compared to Fourier and matrix-pencil estimators, our approach yields lower errors for dynamics with strong dissipation. Overall, these findings suggest that Koopman operator theory provides a practical framework for studying quantum dynamical systems.

I. INTRODUCTION

The control and understanding of open quantum systems has been a central topic to circuit and cavity quantum electrodynamics in recent years [1–3]. An accurate knowledge of oscillation frequencies, dissipation rates and nonlinear interaction strengths enables experimental calibration of quantum devices, as well as validation of master-equation models, which has been of recent interest for quantum computing [4, 5].

In general, such parameters are typically obtained from frequency-domain spectroscopy or nonlinear curve fitting, methods that often require long acquisition times [6]. Fourier and Prony-type techniques such as the matrix-pencil method have also been employed to extract frequencies and decay rates, but their accuracy decreases at strong damping rates [7, 8]. More recently, machine-learning and system-identification methods have been proposed, but these algorithms are typically black boxes lacking of physical interpretability and often rely on large training datasets [9, 10]. Thus, there is a growing need for fast, data-driven techniques capable of inferring Hamiltonian parameters directly from experimental data.

In this work, we aim to contribute to reducing such need by proposing a data-driven framework capable of retrieving Hamiltonian parameters from the dynamics of first-moment observables of open quantum systems. The method relies on the spectrum of the Koopman operator retrieved by using the multiple Hankel Alternative view of Koopman (*mHAVOK*) algorithm [11]. Such a theoretical connection has not been proposed and yet is a necessary step in order to provide a proper justification on why the discrete spectrum of the operator is retrieved

by one of the dynamical matrices built by the method. More importantly, the main contribution of this work relies on showing that such spectrum retrieves Hamiltonian parameters of open quantum systems; an open two-dimensional Quantum Harmonic Oscillator (QHO) was studied as an example. Considering that a closed form of the master equation that governs the evolution of quantum systems cannot be found in real-world experimental settings, the proposed methodology allows for a data-driven spectral-based recovery of the system parameters. For instance, the quadratures could be experimentally measured through homodyne detection [12] and then analyzed through the presented framework with appropriate denoising filters.

The paper is organized as follows: first, Section II provides a mathematical justification on why the spectral analysis performed on *mHAVOK* is equivalent to studying the spectrum of the Koopman operator. Having discussed such a theoretical connection, Section III then introduces the proposed methodology from which one can retrieve Hamiltonian parameters of an open quantum system. Next, Section IV presents a brief theoretical summary on the Lindblad master equation and shows how the open 2D QHO is modeled. Afterward, Sections V and VI provide the results of such simulations, showing how a spectral analysis over first-moment trajectories via the proposed framework allows for a proper reconstruction of Hamiltonian parameters, even for the case of time-dependent Hamiltonians. Finally, Section VII summarizes the current work by presenting the main contributions and limitations found.

II. KOOPMAN - MHAVOK CONNECTION

Consider a smooth classical dynamical system of the form $\dot{\mathbf{x}} = \mathbf{F}(\mathbf{x})$, \mathbf{F} representing the vector field and \mathbf{x} the state vector. The Koopman operator is a linear, infinite-

* juliocesar@tec.mx

dimensional operator that advances in time functions of the state vector known as observables, not to be confused with the observables of quantum mechanics. In practice, we often deal with vector-valued observables $\mathbf{g}(\mathbf{x})$, as we may have multiple observables from our system. If \mathcal{M} is a smooth Riemannian manifold in which the dynamics occur, then they have the following representation:

$$\mathbf{g}(\mathbf{x}) = \begin{bmatrix} g_0(\mathbf{x}) \\ g_1(\mathbf{x}) \\ \vdots \\ g_{p-1}(\mathbf{x}) \end{bmatrix} \in \mathbb{C}^p, \quad (1)$$

The Koopman semigroup $(U^t)_{t \geq 0}$ acts component-wise on \mathbf{g} as follows:

$$(U^t \mathbf{g})(\mathbf{x}) = \mathbf{g}(\Phi^t(\mathbf{x})) = \begin{bmatrix} g_0(\Phi^t(\mathbf{x})) \\ g_1(\Phi^t(\mathbf{x})) \\ \vdots \\ g_{p-1}(\Phi^t(\mathbf{x})) \end{bmatrix}, \quad (2)$$

where Φ^t is the flow map. This semigroup is strongly continuous, thereby allowing for the definition of a generator \mathcal{L} :

$$\mathcal{L}\mathbf{g} := \lim_{t \rightarrow 0} \frac{U^t \mathbf{g} - \mathbf{g}}{t}. \quad (3)$$

Thus, $U^t = e^{t\mathcal{L}}$. For a fixed sampling period $\Delta t > 0$, we define the discrete Koopman operator as

$$U := U^{\Delta t} = e^{\Delta t \mathcal{L}}. \quad (4)$$

Along a given trajectory $\mathbf{x}_k = \Phi^{k\Delta t}(\mathbf{x}_0)$, \mathbf{x}_0 representing the initial condition, we have:

$$\mathbf{g}(\mathbf{x}_{k+1}) = (U\mathbf{g})(\mathbf{x}_k), \quad \mathbf{g}(\mathbf{x}_k) = (U^k \mathbf{g})(\mathbf{x}_0). \quad (5)$$

where Φ^t is the flow map. As detailed in Appendix A and Ref. [11], *m*HAVOK performs a delay embedding on the input data and then rearranges it in a Block Hankel matrix \mathbf{H} . Considering the previous definitions, each column of \mathbf{H} is interpreted as the consecutive action of the Koopman operator on an initial vector of observables \mathbf{h}_0 :

$$\mathbf{H} = [\mathbf{h}_0 \ U\mathbf{h}_0 \ U^2\mathbf{h}_0 \ \dots \ U^{n-m}\mathbf{h}_0]. \quad (6)$$

Equation (6) forms a Krylov sequence whose columns span a corresponding Krylov subspace [13]. In such reference, two strong assumptions were made: 1) the existence of a finite-dimensional subspace of \mathcal{H} invariant under the action of the Koopman operator, and 2) such subspace contains our observable of interest \mathbf{h} . Following this assumption, we assume there exists a Koopman-invariant subspace of dimension k , denoted by \mathcal{K} , and that contains \mathbf{h} .

With this considered, performing an SVD on \mathbf{H} constructs an orthonormal basis, identifying dominant vector-valued observables, i.e., the leading r temporal

modes. A fixed value of r is now assumed; its optimal value is discussed in Subsection A.2. Subsequently, let $\mathcal{H}_P = \text{span}\{\mathbf{v}_0, \dots, \mathbf{v}_{r-1}\}$ denote the finite-dimensional subspace generated by the retained dynamical modes. Two orthogonal projection operators are defined on \mathcal{H} :

$$P : \mathcal{H} \rightarrow \mathcal{H}_P, \quad (7)$$

$$Q : \mathcal{H} \rightarrow \mathcal{H}_Q, \quad (8)$$

where $\mathcal{H}_P \oplus \mathcal{H}_Q = \mathcal{H}$ and $Q = I - P$, I representing the identity operator. Notice how P is a projection over the SVD-derived dominant modes. Hence, every vector-valued observable $\mathbf{g} \in \mathcal{H}$ is uniquely decomposed as

$$\mathbf{g} = P\mathbf{g} + Q\mathbf{g}, \quad (9)$$

with $P\mathbf{g} \in \mathcal{H}_P$ and $Q\mathbf{g} \in \mathcal{H}_Q$. Considering $\mathcal{L} : \mathcal{H} \rightarrow \mathcal{H}$, its action can be decomposed as:

$$\mathcal{L} = I\mathcal{L}I = (P + Q)\mathcal{L}(P + Q), \quad (10)$$

$$= P\mathcal{L}P + P\mathcal{L}Q + Q\mathcal{L}P + Q\mathcal{L}Q. \quad (11)$$

Thus, the projection operator P isolates the part of the observable that lives in the chosen finite-dimensional subspace, while Q collects the residual component. The four blocks in Eq. (11) each describe the action of the generator that (i) stays within \mathcal{H}_P , (ii) maps residual dynamics onto the retained space ($\mathcal{H}_Q \rightarrow \mathcal{H}_P$), (iii) describes how the retained dynamics interact with the orthogonal complement ($\mathcal{H}_P \rightarrow \mathcal{H}_Q$), and (iv) evolves entirely within the residual subspace. The above partition strongly resembles the Mori-Zwanzig formalism from statistical physics, which decomposes the system's dynamics into resolved variables and unresolved components using projection operators, leading to closed equations of motion [14]. Indeed, a connection between Koopman theory and such formalism has already been reported in Ref. [15].

In our case, the projection operators quantify how far the chosen subspace \mathcal{H}_P lies from being Koopman-invariant. Mathematically, the subspace remains invariant under \mathcal{L} when

$$\mathcal{L}\mathcal{H}_P \subseteq \mathcal{H}_P, \quad (12)$$

which happens if and only if

$$P\mathcal{L}Q = Q\mathcal{L}P = 0. \quad (13)$$

If Eq. (13) holds, then $P\mathcal{L}P$ gives an exact finite-dimensional restriction of the Koopman generator on that subspace. In the general case, however, both $P\mathcal{L}Q$ and $Q\mathcal{L}P$ are different from zero, thereby being relevant to properly reconstruct the system dynamics, even if they are not captured in a Koopman-invariant subspace.

With this considered, the regression steps performed in *m*HAVOK (Eqs. (A5) and (A10)) approximate PLP and PLQ , which are simply denoted as \mathbf{A} and \mathbf{B} . Here,

\mathbf{A} captures the linear evolution within the resolved subspace, while \mathbf{B} describes the influence of unresolved components, which appear as forcing. Defining $\mathbf{v} = P\mathbf{g}$ and $\mathbf{u} = Q\mathbf{g}$, the following forced linear model is obtained:

$$\dot{\mathbf{v}} = P\mathcal{L}P\mathbf{v} + P\mathcal{L}Q\mathbf{u}. \quad (14)$$

If $\mathbf{x} = \mathbf{v}$, then we have

$$\dot{\mathbf{x}} = \mathbf{A}\mathbf{x} + \mathbf{B}\mathbf{u}, \quad (15)$$

which is precisely what *mHAVOK* builds, as presented in Eq. (A11). Furthermore, the spectrum of \mathbf{A} represents the spectrum of the Koopman generator restricted to the identified subspace. Let

$$\sigma(\mathbf{A}) = \{\lambda \in \mathbb{C} \mid \det(\mathbf{A} - \lambda I) = 0\} \quad (16)$$

represent the set of retrieved eigenvalues λ_i . This is an important consideration, as the Koopman operator has both a continuous and discrete spectrum. However, \mathbf{A} recovers the discrete spectrum, as, according to Arbabi and Mezic [13], finding a finite-dimensional realization of the Koopman generator on a Koopman-invariant subspace is, in general, equivalent to the existence of the pure point spectrum on that subspace.

It is important to note, however, that the existence of a purely discrete spectrum on a dynamical system is largely a theoretical condition [16]. In practice, the majority of the systems exhibit both a continuous and discrete spectrum. *mHAVOK* overcomes such limitation by allowing the existence of \mathbf{B} , a rectangular matrix that contains information on nonlinear components. Due to its connection with such components, we hypothesize that \mathbf{B} might have a relation with the continuous spectrum. Considering that the spectral analysis of \mathbf{A} alone is sufficient for a proper recovery of Hamiltonian parameters, as will be shown later, such a hypothesis is not pursued in the current work.

III. OVERVIEW OF THE EMPLOYED FRAMEWORK

Having discussed the theoretical connection between Koopman operator theory and the method employed in this work, the methodology pursued in the following is summarized in Fig. 1. We first obtain the expected values of the open quantum system of interest via a numerical solver of the Lindblad master equation [17]. Subsequently, the evolution of such data is provided as input to *mHAVOK*, allowing for 1) retrieving a forced linear model for the system dynamics and 2) employing the spectrum of \mathbf{A} for retrieving Hamiltonian parameters of open quantum systems.

IV. THEORY OF OPEN QUANTUM SYSTEMS

Considering the evolution of the expected values of quantum observables will be analyzed through the afore-

mentioned method, a brief summary on the theory of open quantum systems is now presented.

A. Lindblad master equation

Seminal work published in 1976 by Göran Lindblad introduced the methods by which open quantum systems can be modeled (mainly Born and Markov approximations) [18]. The dynamical equation proposed in his paper has the following form:

$$\frac{d\rho}{dt} = -\frac{i}{\hbar}[H, \rho] + \sum_j \left(L_j \rho L_j^\dagger - \frac{1}{2} \{L_j L_j^\dagger, \rho\} \right), \quad (17)$$

where ρ is the density matrix, H is the Hamiltonian, $\{\cdot, \cdot\}$ denotes the anti-commutator, L_j are jump operators that model system-environment interactions and \cdot^\dagger represents the complex conjugate. A comprehensive derivation of Eq. (17) can be found in Ref. [19]; for a deeper explanation, we refer the reader to Ref. [20].

B. Description of the simulated environment

Throughout this work, an open 2D QHO is modeled using Eq. (17) under a common environment for both the x and y components of the oscillator. The nature of the bath is described as follows:

First, the emission of photons from the system to the bath, also known as a decay, is given by

$$\mathcal{L}_c = a_x + e^{i\phi} a_y, \quad (18)$$

with ϕ being the relative phase between the two system modes and a_i representing the annihilation operator for the i -th component. Physically, the bath does not recognize whether the emission came from the x or y component; it only couples both emissions to the linear combination in Eq. (18). On the other hand, absorption of photons from the bath to the system, a process also known as excitation, is given by \mathcal{L}_c^\dagger .

Additionally, the bath has a temperature $T > 0$ and is considered to be a collection of harmonic oscillators, from which the system can both emit and absorb quanta. The average number of photons in the bath at frequency ω_i is given by the Bose-Einstein distribution [20]:

$$\bar{n}_i(\omega_i, t) = \frac{1}{\exp\left(\frac{\hbar\omega_i}{k_B T}\right) - 1}, \quad (19)$$

where $i = \{x, y\}$ and k_B represents Boltzmann constant. With this considered, the jump operators defined in Eq. (17) are given by

$$L_i^{\text{decay}} := \mathcal{L}_c \sqrt{\kappa(\bar{n}_i + 1)}, \quad (20)$$

$$L_i^{\text{excitation}} := \mathcal{L}_c^\dagger \sqrt{\kappa\bar{n}_i}, \quad (21)$$

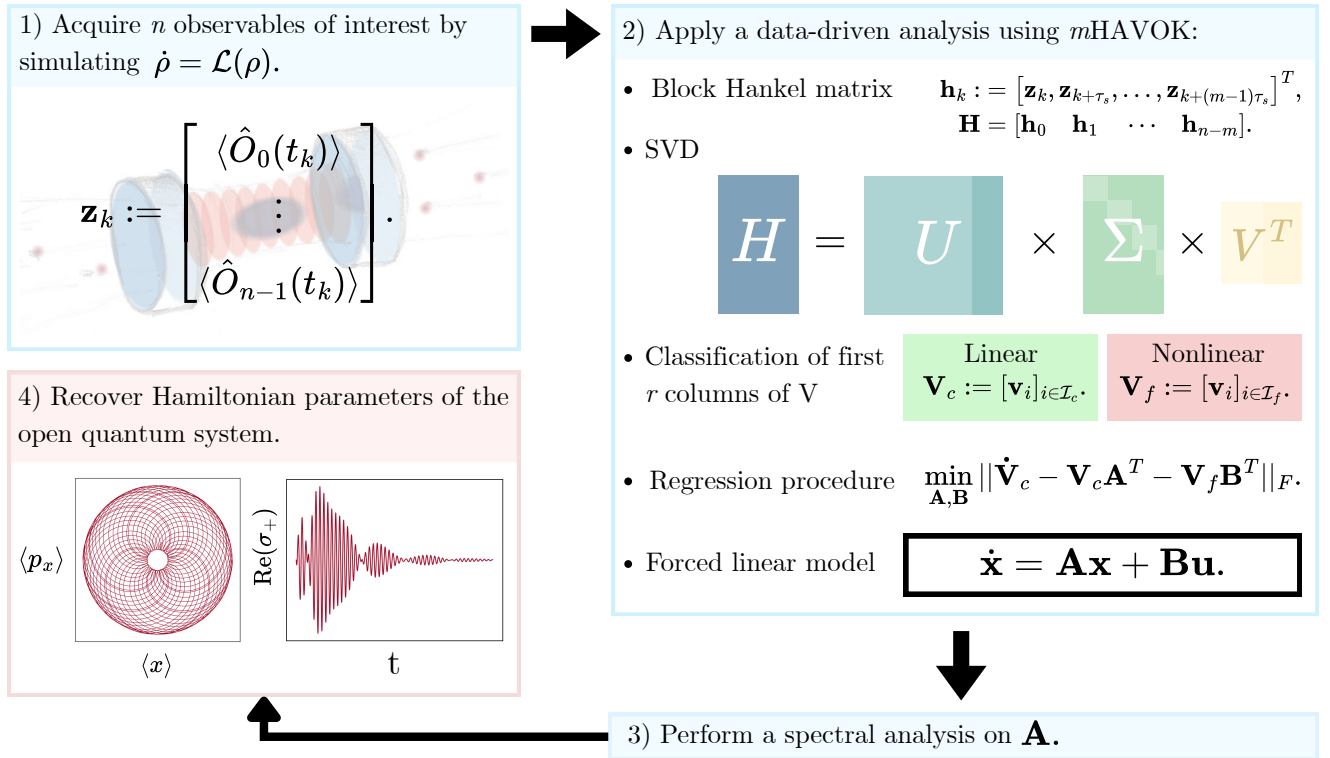


Figure 1. Overview of the pipeline employed in this work. 1) The expected values of observables are first obtained by simulating the Lindblad master equation. 2) Such data is then analyzed through the m HAVOK framework, where two dynamical matrices are retrieved. A spectral analysis is performed on one of them (3), allowing for recovering the discrete spectrum of the Koopman generator and thus Hamiltonian parameters of the open quantum system (4).

with κ being known as the damping rate. Notice how decay holds even if there are no photons in the environment, i.e., there is a vacuum. These phenomena can be attributed to the system's quantum fluctuations [20].

V. RESULTS - TIME-INDEPENDENT HAMILTONIANS

Using QuTiP's solver of Lindblad master equation [17], a coherent state with eigenvalue $\alpha = 1$ was considered as an initial state. Table I summarizes the simulation parameters for obtaining the quadratures of the open oscillator. Having obtained them, the quadrature vector shown in Eq. (23) was provided as input to m HAVOK. The user-defined threshold used in the algorithm for discerning linear from nonlinear components was set to $\tau = 0.95$. Additionally, the embedding dimension equaled $m = 100$, in accordance with prior work on the HAVOK method [11]. These last parameters are part of the m HAVOK input setup, all of them being further discussed in Appendix A.

In the following, a hat in a variable will represent that such parameter was numerically recovered through the spectrum of \mathbf{A} . On the other hand, the real parameter employed in simulating the Lindbladian will not contain any distinctive. With this considered, the percent error

Table I. Simulation parameters employed in this work.

Variable	Value
Simulation time	$t_f = 50$
Time step	$\Delta t = 0.01$
Oscillation frequencies	$\omega_x = 2\pi$ $\omega_y = \pi$
Environment temperature	$T = 2.0$
Damping rate	$\kappa = 0.1$
Fock-state truncations	$n_x = 10$ $n_y = 10$

between both quantities is calculated and denoted as $e_{\lambda\hat{\lambda}}$. Such a metric is compared with traditional well-known methods to recover the oscillation frequencies, such as a Fast Fourier Transformation (FFT) and the generalized pencil-of-function (matrix pencil) method [7], an algorithm capable of extracting damping factors and oscillation frequencies of an input signal, assuming that a sum of complex exponentials serves as a proper basis for it [8].

A. 2D QHO

The Hamiltonian of a two-dimensional quantum harmonic oscillator reads

$$H_0 = \hbar\omega_x a_x a_x^\dagger + \hbar\omega_y a_y a_y^\dagger, \quad (22)$$

where ω_i are the oscillation frequencies and a_i^\dagger denote the creation operators. For notational convenience, the zero of energy has been shifted upward by $\hbar(\omega_x + \omega_y)/2$, merely redefining the energy reference. Throughout this work, the ladder operators, and hence the quadratures, are expressed and studied in dimensionless units.

Considering the Hamiltonian in Eq. (22) is quadratic and the jump operators in Eqs. (20) and (21) are linear, then the Heisenberg equations of motion for the first moments evolve linearly and have closed expressions [20]. Consequently, the evolution of the quadrature vector

$$\mathbf{x} = \begin{bmatrix} \langle x(t) \rangle \\ \langle y(t) \rangle \\ \langle p_x(t) \rangle \\ \langle p_y(t) \rangle \end{bmatrix} \quad (23)$$

is given by the following ordinary differential equation (ODE):

$$\dot{\mathbf{x}} = \mathbf{A}\mathbf{x}, \quad (24)$$

where

$$\mathbf{A} = \begin{bmatrix} -\kappa/2 & \omega_x & 0 & 0 \\ -\omega_x & -\kappa/2 & 0 & 0 \\ 0 & 0 & -\kappa/2 & \omega_y \\ 0 & 0 & -\omega_y & -\kappa/2 \end{bmatrix}.$$

Notice how \mathbf{A} depends on the oscillation frequencies and damping coefficients, but not on the bath occupations \bar{n}_i . With such considerations, Fig. 2 presents the system dynamics for two values of the damping rate κ . In Fig. 2a, the x -mode oscillates twice as fast as the y -mode, in agreement with the simulated oscillation frequencies. Furthermore, the system follows a parabolic Lissajous curve, with the amplitudes decaying and collapsing towards the origin due to the open setup. In contrast, Fig. 2b shows a substantially faster collapse towards the origin resulting from an order-of-magnitude increase in the damping rate. Consequently, no parabolic trajectories are identified.

Regarding the *m*HAVOK framework, the optimal cutoff rank r_{opt} was found to be $r = 4$, which coincides with the number of input observables. This correspondence is not a general feature but rather a consequence of the system's dynamics: since the input quadrature vector obeys the linear ODE in Eq. (24), higher-order modes do not contribute significantly to the reconstructed dynamics.

Having found the optimal cutoff rank, the retrieved dynamical matrix \mathbf{A} was obtained. Up to a Schur decomposition [21], it was found to have the form of A in Eq. (24). Furthermore, its four eigenvalues, up to numerical error,

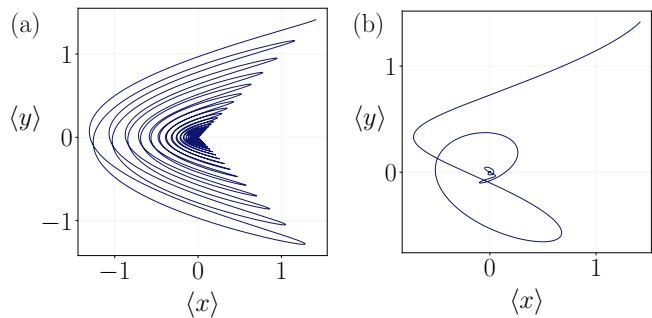


Figure 2. *m*HAVOK's phase-space reconstruction of an open 2D QHO for the x and y components using a damping rate of (a) $\kappa = 0.1$ and (b) $\kappa = 1.0$. No nonlinearities were introduced.

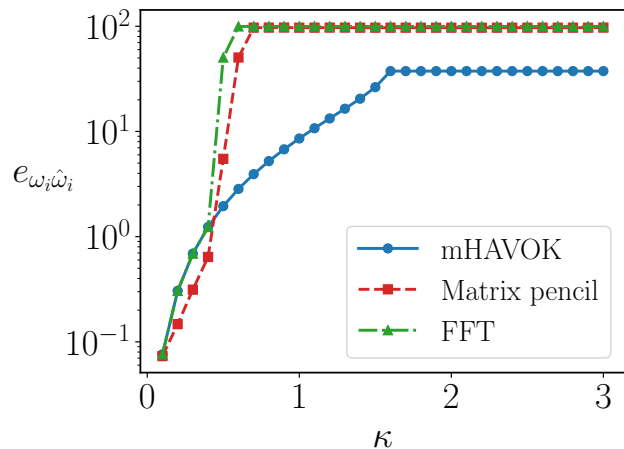


Figure 3. Percent error comparison among three different methods for determining the oscillation frequencies $\hat{\omega}_i$. Our framework exhibits a slower increase in percent error compared to existing alternatives.

came in conjugate pairs of the form $-\hat{\kappa}/2 \pm \hat{\omega}_i$. As discussed in Section II, these eigenvalues correspond to those of the Koopman generator restricted to the invariant subspace spanned by our observables, thereby providing a linear description of the system dynamics.

Once the spectrum of \mathbf{A} was obtained, the percent error between the retrieved Hamiltonian parameters and their true values was calculated. For the case in Fig. 2a where $\kappa = 0.1$, the average percent error between ω_i and $\hat{\omega}_i$ was $e_{\omega_i \hat{\omega}_i} = 0.08\%$, whereas $e_{\kappa \hat{\kappa}} = 7.2 \times 10^{-4}\%$. On the other hand, when increasing 10 times the value of κ in the simulation setup (Fig. 2b), a notable increase is observed in the oscillation-frequency error, with $e_{\omega_i \hat{\omega}_i} = 8.58\%$. Interestingly, the error for the damping rate decreased almost four times once we increased its value, with $e_{\kappa \hat{\kappa}} = 1.8 \times 10^{-4}\%$. Figure 3 compares the percent error associated with three different methods for retrieving the oscillation frequencies as the damping rate increases. Although the matrix-pencil scheme performs better for weak damping rates ($\kappa < 0.5$), *m*HAVOK re-

markably improves the recovery of stronger ones.

B. Kerr nonlinearities

In classical optics, the Kerr effect represents a nonlinear medium whose refractive index has a dependence on the intensity of the field [22]. In quantum mechanics, this effect makes the oscillation frequencies be shifted by an amount proportional to the number of photons at a given time. The Hamiltonian that considers such phenomena is given by [23]:

$$H_{\text{Kerr}} = \hbar \left(\frac{\chi_x}{2} a_x^{\dagger 2} a_x^2 + \frac{\chi_y}{2} a_y^{\dagger 2} a_y^2 + \chi_{xy} n_x n_y \right), \quad (25)$$

with $n_i = a_i a_i^{\dagger}$ representing the number operator and χ_i representing Kerr strength coefficients. The resulting energy spectrum forms an anharmonic ladder [24], with the transition frequency between successive Fock states following $\omega_i + \chi_i n_i$, n_i being a natural number.

Considering Eq. (25) contains quartic terms such as $a_i^{\dagger 2} a_i^2$, the Heisenberg equation of motion for any ladder operator (and hence any quadrature) depends on higher-order moments such as $\langle a^{\dagger} a a \rangle$, preventing closure of moment hierarchy, and hence, a closed expression for their evolution to be obtained [24].

Truncating the Heisenberg equations at first-order moments leads to a time-dependent shift in the oscillation frequency that is proportional to the number operator, capturing the intensity-dependent phase rotation characteristic of the Kerr effect. In the steady state, these effective oscillation frequencies take the form

$$\Omega_x^{\text{eff}} = \omega_x + \chi_x (\langle n_x \rangle_{ss} - 1) + \chi_{xy} \langle n_y \rangle_{ss}, \quad (26)$$

$$\Omega_y^{\text{eff}} = \omega_y + \chi_y (\langle n_y \rangle_{ss} - 1) + \chi_{xy} \langle n_x \rangle_{ss}, \quad (27)$$

with $\langle n_i \rangle_{ss}$ representing the mean value of the number operator of the i -th mode in the steady state.

Kerr nonlinearities were introduced to the simulations with strength parameters set to $\chi_x = 2$, $\chi_y = 3$, while keeping a damping rate $\kappa = 0.1$ and no cross term χ_{xy} . The optimal cutoff rank increased to $r_{\text{opt}} = 20$, almost five times more than the previous case. Considering the value of r_{opt} determines the number of main dynamical modes identified, four out of those 20 were classified as nonlinear. Their appearance can be regarded as a consequence of the lack of a closed-form expression for the evolution of the quadratures, as previously discussed. Although this represents a theoretical limitation, the algorithm is capable of successfully reconstructing the system dynamics through the forced linear model built on the quadratures. Figures 4a and 4c illustrate the reconstructed phase space, showing a spiral trajectory that collapses smoothly toward the origin, with each turn occurring at a slightly different instantaneous frequency, consistent with the presence of a Kerr nonlinearity.

Regarding the retrieval of Hamiltonian parameters, the eigenvalues of \mathbf{A} appeared in complex-conjugate pairs,

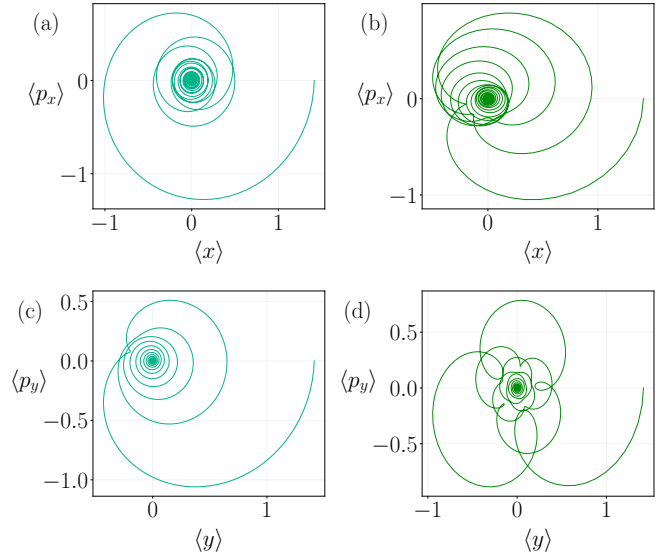


Figure 4. Phase-space reconstruction considering (a-c) $\chi_x, \chi_y = 2, 3$ and (b-d) $\chi_x = \chi_y = 5$. In both cases, the framework successfully recovered Kerr strengths with few numerical errors. No cross-coupling terms were included.

as in the previous case. Their real parts, associated with damping rates, did not exhibit any identifiable pattern. In contrast, the imaginary part followed the relation $\pm(\hat{\omega}_i + n\hat{\chi}_i)$, where $n \in \mathbb{N}$. Hence, *m*HAVOK was capable of recovering Kerr nonlinearity coefficients along with the oscillation frequencies. Such a pattern successfully reproduces the characteristic frequency ladder of Kerr-type nonlinear oscillators.

In order to retrieve the coefficients $\hat{\chi}_i$, the twenty eigenvalues of \mathbf{A} were first sorted by magnitude. For instance, the imaginary parts of the first eight eigenvalues were $\pm\hat{\omega}_y, \pm(\hat{\omega}_y + \hat{\chi}_y), \pm\hat{\omega}_x$, and $\pm(\hat{\omega}_x + \hat{\chi}_x)$. Considering $\omega_y + \chi_y < \omega_x$, the method ordered the imaginary parts starting from the ones associated with the y -mode. Based on this ordering, the Kerr coefficients were estimated by subtracting the absolute values of the imaginary parts of the third and first eigenvalues to obtain χ_y , and similarly, from the seventh and fifth eigenvalues to obtain χ_x . By applying this procedure, the obtained average percent error was $e_{\chi_i \hat{\chi}_i} = 0.04\%$. Additionally, the associated error for the oscillation frequencies remained remarkably low, with $e_{\omega_i \hat{\omega}_i} = 0.02\%$.

In order to observe how the percent error evolves for multiple Kerr strengths, the simulation was performed over a combination of values $(\chi_x = 2 + 0.3n, \chi_y = 3 + 0.2n)$, where $n \in \mathbb{N}$ ranged from 0 to 10. The optimal cutoff rank was calculated for each pair of strengths. Figure 5 illustrates how the percent error is not greater than 5% for all these cases, even in the case where both χ_x and χ_y had a high value (> 3.0). Similarly, the error for recovering the oscillation frequencies for strong nonlinearities remained being lower than 5%. In general, the error tended to increase when $\omega_y + \chi_x \approx \omega_x$, i.e., fre-

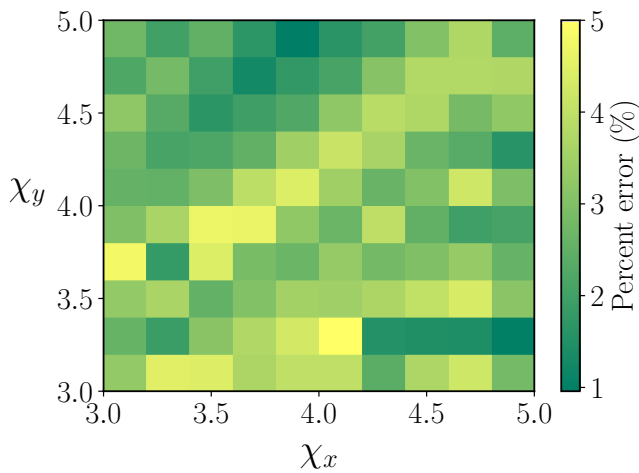


Figure 5. Error comparison for a varying of Kerr nonlinear strengths. The percent error was below 5%, even for strong nonlinearities. To achieve this, the optimal rank r_{opt} was calculated and considered for each simulation.

quencies that are closely spaced needed to be resolved. However, this increase remained relatively low, with the maximum being 4.96% for the case when $\chi_x = 4.1$ and $\chi_y = 3.2$.

As an example, for the case where both $\chi_x = \chi_y = 5$, i.e., strong nonlinearities, the average percent error for Kerr strength parameters was $e_{\chi_i \hat{\chi}_i} = 1.3\%$, while $e_{\omega_i \hat{\omega}_i} = 1.5\%$. Figures 4b and 4d showcase the reconstructed phase space for the aforementioned configuration, where now the trajectories form lobes, each corresponding to an instantaneous variation of the phase due to the amplitude-dependent term $\chi_i \langle n_i(t) \rangle$ earlier discussed.

As a final comparison, we studied whether the algorithm could properly reconstruct the oscillator shown in Figs. 4b and 4d, but under a closed system. Given that *mHAVOK* successfully recovered the quantities of interest for the open system with strong Kerr nonlinearities, one would expect the reconstruction of a closed setup to be straightforward. However, although the reconstruction worked as shown in Figs. 6b and 6d, the method remained remarkably sensitive to the cutoff rank r in contrast to the previous cases, where selecting a rank close to the optimal one tended to yield similar results. This is not generally the case, as illustrated in Figs. 6a and 6c.

1. Retrieving cross-coupling Kerr terms

Subsequently, several cross-term couplings χ_{xy} were simulated while keeping $\chi_x = \chi_y = 0$. In this case, the imaginary part of the eigenvalues of \mathbf{A} took the form $\hat{\Omega}_i = \omega_i + \hat{\chi}_{ij} \langle n_j \rangle$, in agreement with Eqs. (26) and (27). Once the oscillation frequencies $\hat{\omega}_i$ were retrieved, the retrieved $\hat{\chi}_{xy}$ was determined from the above relation. For such purposes, the expected value of the

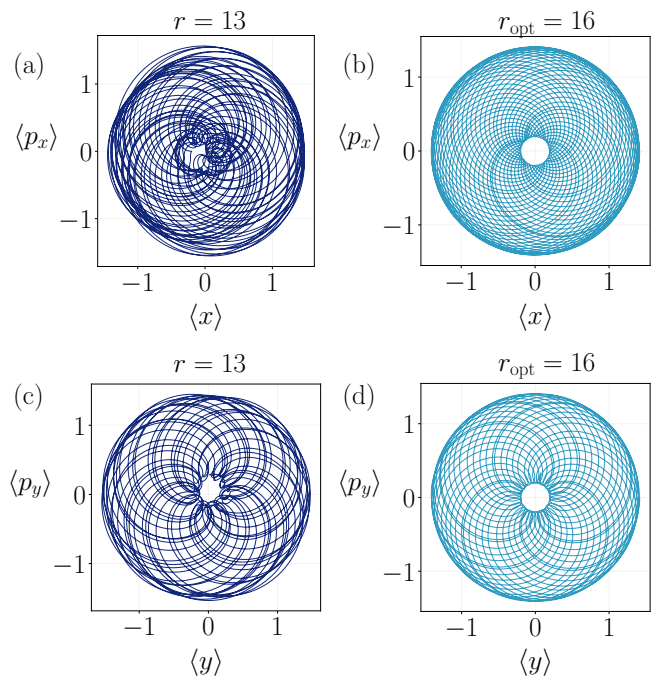


Figure 6. (a-d) Phase-space reconstruction of a closed system considering strong Kerr nonlinearities ($\chi_x = \chi_y = 5$). The dark blue trajectories show the reconstruction using a cutoff rank close to (but not exactly at) the optimal value, while the light blue plots show the reconstruction using the optimal cutoff rank.

Table II. Predicted versus actual values of multiple cross-coupling Kerr nonlinearities.

Real value χ_{xy}	Predicted value $\hat{\chi}_{xy}$
0.05	0.07
0.10	0.09
0.15	0.18
0.20	0.19
0.25	0.15

number operator for both modes was tracked throughout the simulation using QuTiP. By applying this procedure to multiple values of χ_{xy} , Table II summarizes the corresponding results. In general, the method fails to provide an accurate approximation for moderate and strong cross-coupling terms, which can be attributed to the fact that the evolution of the number operator is not properly reconstructed by the forced linear model of *mHAVOK*. Consequently, the retrieved oscillation frequencies are only approximated by the value of the number operator in the steady state.

C. Jaynes-Cummings interaction

The Jaynes-Cummings model describes the interaction between a two-system atom, i.e., a qubit, and a single mode of the electromagnetic field [25]; in this work, a coupling on the x -mode of the electromagnetic field is assumed and studied. With this considered, the qubit can be found in either the ground state $|g\rangle$ with energy E_g , or in the excited state $|e\rangle$ with energy E_e . Mathematically, its Hamiltonian is given by

$$\begin{aligned} H_{JC} &= H_{\text{atom}} + H_{\text{interaction}}, \\ &= \frac{\Omega}{2}\sigma_z + g\hbar(a_x\sigma_+ + a_x^\dagger\sigma_-), \end{aligned} \quad (28)$$

where $\Omega \equiv E_e - E_g$, g represents the coupling strength, σ_z is the third Pauli matrix, and (σ_+, σ_-) represent, respectively, the raising and lowering qubit operators. Additionally, the qubit can spontaneously emit a photon and end up in the ground state. This procedure is known as relaxation and is modeled through a jump operator of the form [26]

$$L^{\text{relaxation}} = \sqrt{\gamma}\sigma_-, \quad (29)$$

where γ is the relaxation rate. Similarly, the process from which the qubit's coherence decays is known as dephasing. If γ_ϕ represents the dephasing rate, then this process is represented by the jump operator [26]

$$L^{\text{dephasing}} = \sqrt{\gamma_\phi}\sigma_z. \quad (30)$$

In this case, the equation of motion for the annihilation operator is coupled with the qubit lowering operator σ_- . Assuming the atom remains mostly in the ground state allows us to approximate $\sigma_z \approx 1$, leading to the linear set of equations

$$\begin{pmatrix} \dot{a} \\ \dot{\sigma}_- \end{pmatrix} = -i \begin{pmatrix} \omega_x & g \\ -g & \omega_q \end{pmatrix} \begin{pmatrix} a \\ \sigma_- \end{pmatrix}. \quad (31)$$

The eigenvalues of this matrix yield the dressed frequencies that describe the oscillations of the combined qubit-cavity system [25]. Mathematically,

$$\omega_\pm = \frac{1}{2} \left[(\omega_q + \omega_x) \pm \sqrt{4g^2 + \Delta^2} \right], \quad (32)$$

with ω_q being the qubit frequency and $\Delta \equiv \omega_q - \omega_x$ representing the detuning, i.e., how far apart both oscillators are in frequency [26].

Along with the simulation parameters presented in Table I, the Jaynes-Cummings interaction was simulated with the qubit's initial state being $|g\rangle$ and an oscillation frequency $\omega_q = 2\pi$. The coupling strength was set to $g = 0.15$, while the relaxation and dephasing rates were, respectively, $\gamma = 0.1$ and $\gamma_\phi = 0.01$. For this case,

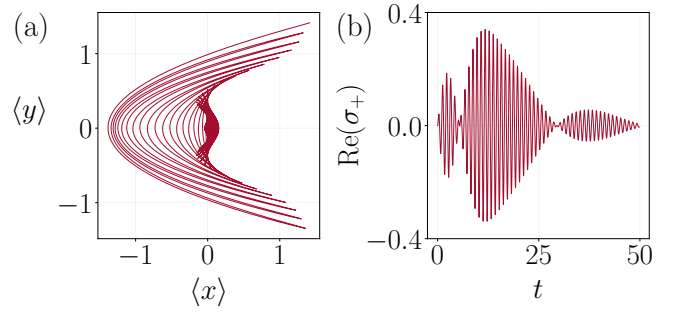


Figure 7. (a) Phase-space reconstruction under a Jaynes-Cummings interaction. (b) Retrieved evolution of $\langle\sigma_+(t)\rangle$ via *mHAVOK*'s forced linear model.

mHAVOK was provided with the observables

$$\mathbf{x}' = \begin{bmatrix} \langle x(t) \rangle \\ \langle p_x(t) \rangle \\ \langle y(t) \rangle \\ \langle p_y(t) \rangle \\ \langle \text{Re}(\sigma_+)(t) \rangle \\ \langle \text{Im}(\sigma_+)(t) \rangle \end{bmatrix}. \quad (33)$$

Figure 7a illustrates how the forced linear model successfully reconstructs the parabolic Lissajous curves with decaying amplitudes, but, in contrast to Fig. 2, the parabola does not exhibit a collapse but rather a change in its orientation due to the qubit-field interaction. Additionally, the evolution of the raising qubit operator is also recovered and visualized in Fig. 7b, where coherent Rabi oscillations are showcased in initial times; the long-time behavior showcases a decay on them, which is explained by the gradual loss of energy and coherence via the jump operators. The optimal cutoff rank was found at $r = 20$, where, interestingly, all the identified components were classified as linear.

Furthermore, the imaginary part of the eigenvalues of \mathbf{A} allowed for retrieving the dressed frequencies defined in Eq. (32). Solving for $g = 0.15$ in the aforementioned equation, a retrieved value $\hat{g} = 0.13$ was obtained, yielding a percent error $e_{g\hat{g}} = 13.33\%$. These results were sensitive to moderate-strong dephasing and relaxation rates. However, they improved substantially when the qubit frequency was not a multiple or exactly equal to ω_x . For instance, choosing $\omega_q = \pi/e$ resulted in an estimate of $\hat{g} = 0.16$, which has an associated percent error $e_{g\hat{g}} = 6.67\%$, half of the obtained when $\omega_q = 2\pi$. This can be attributed to the fact that when both frequencies coincide, the system is in resonance, making it more challenging to accurately identify the coupling strength.

Sweeping over multiple values of g , the method accurately recovered only weak and moderate coupling strengths. For example, for $g = 0.25$, the method recovered $\hat{g} = 0.28$, yielding a percent error $e_{g\hat{g}} = 12.00\%$. However, when doubling the coupling strength to $g = 0.50$, the method yielded a percent error of 26%. Therefore, the algorithm provides a reasonable estimation of

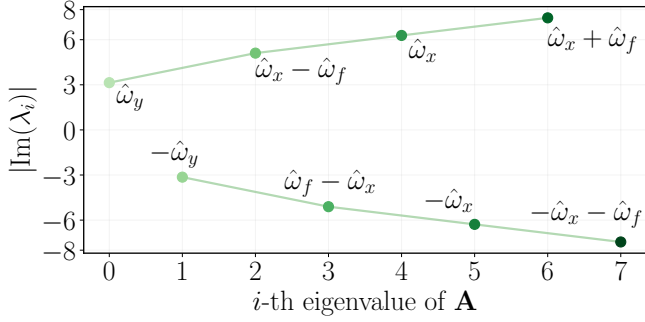


Figure 8. Evolution of the imaginary part of the eigenvalues of \mathbf{A} , which are denoted as λ_i . Complex-conjugate pairs are obtained, each representing a linear combination of the oscillation frequencies ω_x , ω_y and ω_f .

the coupling parameter when the qubit frequency is not close to the oscillation frequency of the field, and the coupling strength remains within the weak-to-moderate regime.

VI. RESULTS - TIME-DEPENDENT HAMILTONIAN

Along with H_0 defined in Eq. (22), a time-dependent Hamiltonian with a modulation frequency on the x -mode is now studied. Mathematically, it has the following form:

$$H_f(t) = \delta \cos(\omega_f t) a_x^\dagger a_x, \quad (34)$$

where δ denotes the modulated amplitude and ω_f the modulated frequency. Considering such Hamiltonian, the ladder operator, and hence the quadratures, evolve as

$$\langle a_x(t) \rangle = \langle a_x(0) \rangle e^{-\kappa t/2} \sum_{m=-\infty}^{\infty} J_m\left(\frac{\delta}{\omega_f}\right) e^{-i(\omega_x + m\omega_f)t}. \quad (35)$$

Equation (35) exhibits sidebands at $\omega_x + m\omega_f$ weighted by the Bessel coefficients $J_m(\delta/\omega_f)$. In the presence of Kerr and cross-Kerr terms, these sidebands are shifted by the effective frequencies Ω_i^{eff} , combining the effects of frequency and intensity-dependent phase rotations.

Simulating the modulated amplitude $\delta = 4$ and modulated frequency $\omega_f = \pi/e$, the algorithm successfully recovered $\hat{\omega}_f$ within 1.74% of their true value. Figure 8 shows how the imaginary part of the spectrum grows and recovers all the oscillation frequencies, even in the presence of time-dependent Hamiltonians. These can be identified as the expected sidebands presented in Eq. (35). Moreover, as detailed in Section II, their appearance can be interpreted as eigenvalues of the Koopman generator restricted to our space of quantum observables, and whose realization is given by \mathbf{A} . This allows us to span a Koopman-invariant subspace from the observables, providing a linear and well-behaved evolution of the dynamics, even in the presence of time-dependent parameters.

To achieve this, all relevant frequencies must be captured, which is indeed the case.

As a limitation, the method failed for retrieving ω_f when strong modulation coefficients were considered ($\delta > 3$). For instance, when the modulation amplitude was increased to $\delta = 10$, the spectrum exhibited no recognizable pattern. One of the retrieved frequencies was identified as $\hat{\omega}_y$ with a 0.06% error. However, the preceding and following frequencies could not be expressed as a linear combination of $\hat{\omega}_x$ or $\hat{\omega}_f$. Considering increasing δ increases the contribution of more Bessel functions in Eq. (35), multiple neighboring and closely spaced sidebands appear. Hence, the algorithm cannot isolate and retrieve the modulated frequency $\hat{\omega}_f$. Nevertheless, the forced linear model can still reconstruct the system dynamics, primarily because of the additional nonlinear dimensions captured in \mathbf{B} , which are associated with such multiple Bessel functions. Despite this, the model fails to correctly retrieve the modulated frequency.

VII. CONCLUSIONS

A novel method for retrieving Hamiltonian parameters of open quantum systems is presented, with the studied system being an open 2D QHO. By constructing a forced linear model for the expected value of first-moment observables, spectral analysis successfully recovers oscillation frequencies, damping rates, and Kerr nonlinearities, even when considering time-dependent Hamiltonians. Also, a decent though not optimal estimation is obtained for recovering coupling strengths of a Jaynes-Cummings interaction. Most recovered parameters deviate by less than 5% from their true values, with a maximum deviation of 15% observed in one of the Jaynes-Cummings coupling strengths. In these particular cases, the proposed framework identified a larger number of nonlinear components, thereby increasing its influence on the system dynamics. Since the spectral analysis is performed on the dynamical matrix that best captures the evolution of the linear components, a slight decrease in the accuracy of parameter retrieval is expected. In general, the matrix describing the nonlinear components is rectangular, which precludes performing a spectral analysis on it.

An advantage of the algorithm is its ability to recover strong damping rates, even in the presence of nonlinearities. This value was increased by almost an order of magnitude and was still successfully recovered, at least in the case where neither Kerr nonlinearities nor Jaynes-Cummings interactions were introduced. Additionally, the method was compared with the FFT and matrix-pencil schemes for recovering oscillation frequencies and damping rates, outperforming both of them for strongly damped cases and yielding equivalent results in other regimes.

The method relies on Koopman operator theory to successfully reconstruct the system dynamics, where one of

the dynamical matrices represents a finite-dimensional realization of the Koopman generator onto a Koopman-invariant subspace spanned by the expected values of the observables. To the best knowledge of the authors, this theoretical connection has not been previously reported. Therefore, these results motivate further exploration of Koopman theory as a practical framework for analyzing quantum dynamical systems.

VIII. ACKNOWLEDGMENTS

We acknowledge fruitful discussions with Dr. Oliver Probst's research group (webpage). Also, we thank the anonymous reviewers for their valuable feedback.

Appendix A: On the Hankel Alternative view of Koopman (HAVOK) method

The HAVOK algorithm was originally introduced as a method to study classic nonlinear dynamical systems via forced linear models [27]. The methodology was mainly employed on attractors and worked by making use of Takens' embedding theorem, which guarantees a diffeomorphic attractor from delay embeddings of a function of the system's state variables [28]. Although HAVOK successfully reconstructs several dynamical systems, multiple limitations have been identified [29, 30]: first, only one function of the system's state variables could be provided as input. Second, out of the r main dynamical modes identified in the schema, it was arbitrarily assumed the system's forcing only came from the r -th mode. Third, no objective criterion for selecting such r was provided.

The aforementioned limitations were recently addressed in a novel methodology named as m HAVOK [11]. The proposed extension allowed the method to include multiple time measurements, included a framework for identifying linear and forcing terms among the main r dynamical modes, and presented an objective criterion for selecting r . Such improvements remarkably improved the reconstructed dynamics, even in complex nonlinear systems. In the following, an explanation of how m HAVOK works is presented; for a thorough discussion of it, we direct the reader to Ref. [11].

1. Review of the m HAVOK algorithm.

Consider the evolution of the expected values of observables of a (possibly nonlinear) dynamical system. In this work, we are studying the expected values of n quantum observables stacked in a vector \mathbf{z}_k ,

$$\mathbf{z}_k := \begin{bmatrix} \langle \hat{O}_0(t_k) \rangle \\ \vdots \\ \langle \hat{O}_{n-1}(t_k) \rangle \end{bmatrix}, \quad (\text{A1})$$

where $k \in \mathbb{N}$. The method performs a delay embedding on \mathbf{z}_k as follows:

$$\mathbf{h}_k := [\mathbf{z}_k, \mathbf{z}_{k+\tau_s}, \dots, \mathbf{z}_{k+(m-1)\tau_s}]^T, \quad (\text{A2})$$

where m is the embedding dimension and $\tau_s = 1$ is known as the delay time. All \mathbf{h}_k are stored in a block Hankel matrix,

$$\mathbf{H} = [\mathbf{h}_0 \quad \mathbf{h}_1 \quad \dots \quad \mathbf{h}_{n-m}]. \quad (\text{A3})$$

Then, a thin Singular Value Decomposition (SVD) [31] is performed,

$$\mathbf{H} = \mathbf{U}_l \mathbf{S}_l \mathcal{V}_l^T, \quad (\text{A4})$$

where $l = \min(m, n - m + 1)$. The first r columns of \mathcal{V}_l^T are retained; let \mathbf{V} denote this new matrix and r be referred to as the cutoff rank. With this considered, a first regression procedure is performed on \mathbf{V} in order to obtain \mathbf{C} , which is defined as the matrix that minimizes

$$\min_{\mathbf{C}} \|\dot{\mathbf{V}} - \mathbf{V}\mathbf{C}^T\|_F, \quad (\text{A5})$$

with $\|\cdot\|_F$ denoting the Frobenius norm and $\dot{\mathbf{V}}$ the temporal derivative of \mathbf{V} . Afterward, the coefficient of determination between each of the columns of $\dot{\mathbf{V}}$ and $\mathbf{V}\mathbf{C}$ is performed,

$$R_i^2 = 1 - \frac{\|\dot{\mathbf{v}}_i - \mathbf{V}\mathbf{c}_i\|^2}{\|\dot{\mathbf{v}}_i - \bar{v}_i \cdot \mathbf{1}\|^2}, \quad (\text{A6})$$

where $(\mathbf{c}_i, \dot{\mathbf{v}}_i)$ are, respectively, the i -th columns of \mathbf{C} and $\dot{\mathbf{V}}$, $\|\cdot\|$ denotes the Euclidean norm in L^2 , \bar{v}_i is the temporal mean of $\dot{\mathbf{v}}_i$ and $\mathbf{1}$ is a vector of ones. Each of the r columns of \mathbf{V} is classified as linear or nonlinear according to their R^2 value:

$$\mathcal{I}_c := \{i : R_i^2 \geq \tau\}, \quad (\text{A7})$$

$$\mathcal{I}_f := \{1, \dots, r\} \setminus \mathcal{I}_c, \quad (\text{A8})$$

with τ being a user-defined threshold and $(\mathcal{I}_c, \mathcal{I}_f)$ representing, respectively, the index sets of linear and nonlinear dimensions. If \mathbf{v}_i is the i -th column of \mathbf{V} , then such components are separated into two different matrices:

$$\mathbf{V}_c := [\mathbf{v}_i]_{i \in \mathcal{I}_c}, \quad \mathbf{V}_f := [\mathbf{v}_i]_{i \in \mathcal{I}_f}. \quad (\text{A9})$$

Next, a second regression problem is defined in order to obtain two new matrices; each of them models, respectively, the evolution of linear (**A**) and nonlinear (**B**) components. Mathematically,

$$\min_{\mathbf{A}, \mathbf{B}} \|\dot{\mathbf{V}}_c - \mathbf{V}_c \mathbf{A}^T - \mathbf{V}_f \mathbf{B}^T\|_F, \quad (\text{A10})$$

where $\mathbf{A} \in \mathbb{C}^{|\mathcal{I}_c| \times |\mathcal{I}_c|}$ and $\mathbf{B} \in \mathbb{C}^{|\mathcal{I}_c| \times |\mathcal{I}_f|}$ and $|\cdot|$ denoting the cardinality of the sets. Subsequently, the following forced linear system is numerically solved:

$$\dot{\mathbf{x}} = \mathbf{A}\mathbf{x} + \mathbf{B}\mathbf{u}, \quad (\text{A11})$$

with $\mathbf{u} := \mathbf{V}_f$ and \mathbf{x} representing the simulated state vector. The initial condition $\mathbf{x}(0)$ is a column vector given by the first row of \mathbf{V}_c . Finally, the simulated block Hankel matrix $\hat{\mathbf{H}}$ is retrieved by reapplying the SVD factorization:

$$\hat{\mathbf{H}} = \mathbf{U}_c \mathbf{\Sigma}_c \mathbf{x}^T, \quad (\text{A12})$$

where \mathbf{U}_c and $\mathbf{\Sigma}_c$ represent the SVD matrices of the linear components. The reconstructed observables defined in Eq. (A1) will be given by the first block of $\hat{\mathbf{H}}$. With this procedure, *m*HAVOK provides a forced linear model that allows for obtaining such quantities of interest.

2. On the identification of the optimal cutoff rank

The optimal cutoff rank r_{opt} is identified by calculating the condition number of the dynamical matrix \mathbf{B} [11], which is defined as the quotient between its highest and lowest singular values [32]. Mathematically,

$$\kappa(\mathbf{B}) := \frac{\sigma_{\max}(\mathbf{B})}{\sigma_{\min}(\mathbf{B})}, \quad (\text{A13})$$

with $\sigma_{\max}(\cdot)$ and $\sigma_{\min}(\cdot)$ each representing the maximum and minimum singular values of \mathbf{B} . Physically, this value represents an optimal, non-redundant choice of dynamical modes from which the system can successfully build a forced linear model of the system dynamics. In general, exceeding such value may lead to overfitting, while not reaching it may prevent crucial dynamical modes from being perceived, precluding a successful reconstruction from being obtained. The condition number, being an indicator of how sensible a matrix is to changes in its input [32], successfully captures these phenomena, therefore being an objective criterion for the cutoff rank selection.

Considering each choice of r has an associated \mathbf{B} , the condition number was calculated over a sweep of values $[r_{\min}, r_{\max}]$, with r_{\min} being the minimum number from which *m*HAVOK identified at least one linear dimension and $r_{\max} = 30$ an arbitrary upper value. The optimal rank employed throughout this work was the one that had the highest condition number within the selected interval.

Appendix B: Computational requirements demanded by *m*HAVOK

Considering an input of C vector-valued of observables, each of length N , an embedding dimension m , and a cutoff rank r in the SVD procedure, the computational cost of *m*HAVOK is

$$O[mC(n - m)] + O[mC(N - m) \min(mC, n - m)] + O[(N - m)r^2 + r^3]. \quad (\text{B1})$$

The first term corresponds to the construction of the Block Hankel matrix, the second to its SVD factorization,

and the third to the regression procedures and the state-space simulation of the forced linear model. In practice, $N \gg mC$ and the SVD term dominates. Hence, the time complexity reduces to $O[(mC)^2 N]$, increasingly quadratically with the embedding dimension and linearly with the length of each vector-valued observable.

-
- [1] D. Sank, A. Opremcak, A. Bengtsson, M. Khezri, Z. Chen, O. Naaman, and A. Korotkov, System characterization of dispersive readout in superconducting qubits, *Phys. Rev. Appl.* **23**, 024055 (2025).
- [2] P. Binder and D. Braun, Quantum parameter estimation of the frequency and damping of a harmonic oscillator, *Phys. Rev. A* **102**, 012223 (2020).
- [3] A. Blais, A. L. Grimsmo, S. M. Girvin, and A. Wallraff, Circuit quantum electrodynamics, *Rev. Mod. Phys.* **93**, 025005 (2021).
- [4] H. Zhang, B. Pokharel, E. Levenson-Falk, and D. Lidar, Predicting non-Markovian superconducting-qubit dynamics from tomographic reconstruction, *Phys. Rev. Appl.* **17**, 054018 (2022).
- [5] H. Kamakari, S.-N. Sun, M. Motta, and A. J. Minnich, Digital quantum simulation of open quantum systems using quantum imaginary-time evolution, *PRX Quantum* **3**, 010320 (2022).
- [6] J. H. M. Jensen and K. Mølmer, Gaussian theory for estimating fluctuating perturbations with backaction-evading oscillator variables, *Phys. Rev. A* **106**, 022613 (2022).
- [7] T. K. Sarkar and O. Pereira, Using the matrix pencil method to estimate the parameters of a sum of complex exponentials, *IEEE Antennas Propag. Mag.* **37**, 48 (1995).
- [8] Y. Hua and T. K. Sarkar, Matrix pencil method for estimating parameters of exponentially damped/undamped sinusoids in noise, *IEEE Trans. Acoust. Speech Signal Process.* **38**, 814 (1990).
- [9] C. Pira, Lirandë; Ferrie, On the interpretability of quantum neural networks, *Quantum Machine Intelligence* **6**, 52 (2024).
- [10] I. A. Luchnikov, E. O. Kiktenko, M. A. Gavreev, H. Ouerdane, S. N. Filippov, and A. K. Fedorov, Probing non-markovian quantum dynamics with data-driven analysis: Beyond “black-box” machine-learning models, *Phys. Rev. Res.* **4**, 043002 (2022).
- [11] C. Colchero, J. Perez, A. Herrera, and O. Probst, A multichannel generalization of the HAVOK method for the analysis of nonlinear dynamical systems (2025), submitted to *Chaos*, arXiv:2509.13424 [nlin.CD].
- [12] A. I. Lvovsky and M. G. Raymer, Continuous-variable optical quantum-state tomography, *Rev. Mod. Phys.* **81**, 299 (2009).
- [13] H. Arbabi and I. Mezić, Ergodic theory, Dynamic Mode Decomposition, and computation of spectral properties of the Koopman operator, *SIAM J. Appl. Dyn. Syst.* **16**, 2096 (2017).
- [14] R. Zwanzig, *Nonequilibrium Statistical Mechanics* (Oxford University Press, 2001).
- [15] Y. T. Lin, Y. Tian, D. Livescu, and M. Anghel, Data-driven learning for the Mori–Zwanzig formalism: A generalization of the Koopman learning framework, *SIAM J. Appl. Dyn. Syst.* **20**, 2558 (2021).
- [16] G. Haller and B. Kaszás, Data-driven linearization of dynamical systems, *Nonlinear Dynamics* **112**, 18639 (2024).
- [17] J. R. Johansson, P. D. Nation, and F. Nori, QuTiP: An open-source Python framework for the dynamics of open quantum systems, *Comput. Phys. Commun.* **183**, 1760 (2012).
- [18] G. Lindblad, On the generators of quantum dynamical semigroups, *Commun. Math. Phys.* **48**, 119 (1976).
- [19] D. Manzano, A short introduction to the Lindblad master equation, *AIP Adv.* **10**, 025106 (2020).
- [20] H.-P. Breuer and F. Petruccione, *The Theory of Open Quantum Systems* (Oxford University Press, 2007).
- [21] R. Horn and C. Johnson, *Matrix Analysis* (Cambridge University Press, 2012).
- [22] D. Walls and G. Milburn, *Quantum Optics* (Springer Berlin Heidelberg, 2008).
- [23] C. A. Milburn, G. J.; Holmes, Quantum coherence and classical chaos in a pulsed parametric oscillator with a Kerr nonlinearity, *Phys. Rev. A* **44**, 4704 (1991).
- [24] H. J. Carmichael, *Statistical Methods in Quantum Optics 2: Non-Classical Fields*, 1st ed., Theoretical and Mathematical Physics (Springer Berlin, Heidelberg, 2008).
- [25] E. T. Jaynes and F. W. Cummings, Comparison of quantum and semiclassical radiation theories with application to the beam maser, *Proc. IEEE* **51**, 89 (1963).
- [26] J. Larson and T. Mavrogordatos, *The Jaynes–Cummings Model and Its Descendants*, 2053-2563 (IOP Publishing, 2021).
- [27] S. L. Brunton, B. W. Brunton, J. L. Proctor, E. Kaiser, and J. N. Kutz, Chaos as an intermittently forced linear system, *Nat. Commun.* **8**, 19 (2017).
- [28] F. Takens, Detecting strange attractors in turbulence, in *Dynamical Systems and Turbulence, Warwick 1980*, edited by D. Rand and L.-S. Young (Springer, Berlin, Heidelberg, 1981) pp. 366–381.
- [29] X. Cai and Y. Qian, Detection and reconstruction of bursting oscillations in complex systems using the HAVOK analysis framework, *Algorithms* **17**, 10.3390/a17090388 (2024).
- [30] J. Yang, J. Zhao, J. Song, J. Wu, C. Zhao, and H. Leng, A hybrid method using HAVOK analysis and machine learning for predicting chaotic time series, *Entropy* **24**, 10.3390/e24030408 (2022).
- [31] J. Demmel, 6. Singular Value Decomposition, in *Templates for the Solution of Algebraic Eigenvalue Problems* (SIAM, 2000) pp. 135–147.
- [32] A. K. Cline, C. B. Moler, G. W. Stewart, and J. H. Wilkinson, An estimate for the condition number of a matrix, *SIAM J. Numer. Anal.* **16**, 368 (1979).